Compton Imaging with Scintillators in a Virtual Geant4 Space

Thesis Submitted in Partial Fulfilment of the Requirements for the Degree of B.Sc. in Physics

Author:
Tim Almqvist

Supervisors:
Dr. Luis Sarmiento and Prof. Dirk Rudolph

LUND
UNIVERSITY

Department of Physics
Division of Nuclear Physics

January, 2015

Abstract

In this study the Geant4 toolkit has been used to perform Monte Carlo simulations of relatively inexpensive, inorganic, scintillator-based detectors. Full simulations of the optical photons produced via the scintillation process have been done in order to achieve realistic responses from the attached electro-optical sensors.

The main focus of this work is on identifying interaction positions in scintillator bars from the readouts of the electro-optical sensors attached to them. A handful of configurations of electro-optical sensors have been simulated. Position accuracies down to approximately 8 mm, corresponding to 8% of the length of the scintillator bar, have been achieved in these simulations.

Although the concept of the imaging algorithm described in section 5 is rather simple, it requires careful implementation. Due to time constraints this imaging is yet to be realised.

Acknowledgements

I would like to thank Dr. Luis Sarmiento for being an awesome person whom I look up to. Not only has he guided me through the process of learning to work with Geant4 and answer all of my numerous questions, but he has also taught me a huge amount of things which definitely will be very useful in the future. He also helped me out many times with both writing and programming. I do hope I get the opportunity to learn more from you in the future.

Secondly I would like to thank Prof. Dirk Rudolph for noticing my interest in programming, simulations, and computers, and for offering me this great opportunity of doing my bachelors work here. Also during the project he provided informative explanations and discussions, as well as a lot of help and feedback during the writing process.

Further, I want to thank Natasa Lalovic for providing information about the scintillators and the imaging techniques. And Pavel Golubev for showing me the physical components which I were simulating, and providing information about the electro-optical sensors.

List of Acronyms

PMT	Photomultiplier tube
CsI	Caesium iodide
CsI(Na)	Sodium doped caesium iodide
CsI(Tl)	Thallium doped caesium iodide
SiPM	Silicon photomultiplier
ESR	Enhanced specular reflector
ID	Identification number

Contents

1 Introduction **1**

2 Physics Background **2**
2.1 Interactions of Photons with Matter 2
2.2 Scintillating Materials 4
2.3 Electro-Optical Sensors 5
2.4 The Setup 6
2.5 Monte-Carlo Methods 7
2.6 The `Geant4` Toolkit 7

3 Simulations with `Geant4` **8**
3.1 Geometries 8
3.2 Geometry of the Detector Setup 9
3.3 Materials 10
3.4 Physics Processes 11
3.5 Recording Data 13

4 Position Resolution in the Scintillator Bars **15**
4.1 Photomultiplier Tubes 15
4.2 Four Silicon Photomultipliers on One Side 17
4.3 Eight SiPMs, Four in Each End 19
4.4 Eight SiPMs on the Sides 21
4.5 Further Analysis of Two Configurations 23
4.6 Position in the x-y Plane 25

5 Imaging Algorithm **27**

6 Summary and Outlook **27**

1 Introduction

Gamma imaging is the technique of identifying the origin of a γ-ray emitting sample, by exploiting the properties of Compton scattering. The technique relies on identifying interaction points of individual γ-rays, and its energy deposition. When position and energy deposition have been identified, it is possible to estimate the origin of the γ-rays in three-dimensional space.

Gamma imaging techniques have a wide variety of applications including, for instance, medical imaging and homeland security. Further, these techniques can be used during nuclear physics experiments for rejecting background which could not have originated from the source of interest. This is valuable for any high-precision experiment, and especially for experiments with low reaction rates.

In this study relatively inexpensive γ imaging detectors, based on inorganic scintillators, have been explored through simulations. The considered setup consists of six scintillator bars positioned in two layers, followed by a 5×5 array of scintillator detectors, intended to fully absorb incident γ-rays.

An application using the Geant4 toolkit has been created for performing simulations. All optical photons, produced by the scintillating materials are simulated in order to obtain realistic responses of the electro-optical sensors. The sensors employed are photomultiplier tubes, and silicon photomultipliers.

Four different configurations of electro-optical sensors, attached to scintillator bars, have been simulated, and their resolution of interaction positions have been evaluated. Gamma-ray energies of 511 keV were used in the simulations, as they are produced by electron-positron annihilations, which are common in all β^+-active samples.

With γ-ray energies of 511 keV it is expected to most frequently achieve one Compton scattering event prior to absorption in the full detector setup. The concept for performing the analysis and imaging for the setup is discussed in section 5. Although it is not difficult conceptually, it requires careful implementation practically. Due to time constraints, simulations and analyses of the full setup were found to be beyond the scope of a bachelor thesis.

In section 2 the physics background that is relevant for the detector setup and imaging techniques are discussed. Section 3 presents the details of the simulations, such as geometries and properties of the components, physics processes and how data was recorded. In section 4 the obtained data is analysed and position resolutions are discussed. How imaging can be performed is discussed briefly in section 5. Finally, a summary and an outlook is given in section 6.

2 Physics Background

2.1 Interactions of Photons with Matter

There are three main processes with which γ-rays interact with matter: the photoelectric effect, Compton scattering, and pair production [1]. Each one of these dominates in different regions of the energy spectrum of γ-rays, as shown in figure 2.1.

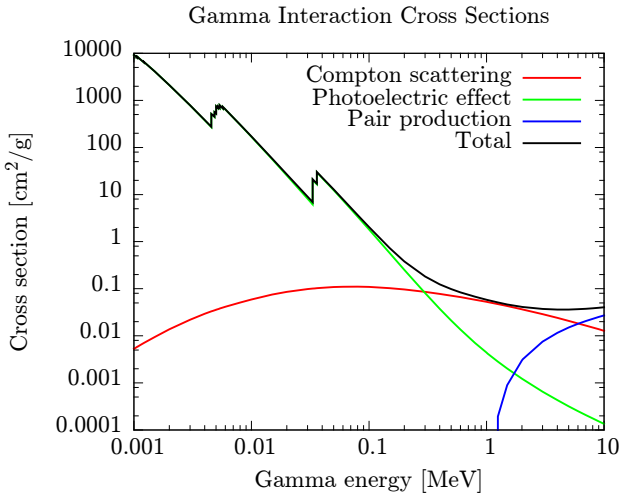

Figure 2.1: Gamma-ray interaction cross sections for caesium iodide as a function of γ-ray energy [2].

The photoelectric effect has the highest cross section for γ-rays at energies up to a few hundred keV. Through the photoelectric process effectively all of the γ-ray energy, E_γ, is absorbed by a single electron. A small amount of energy is shared with the nucleus of the atom due to linear momentum conservation, but this is negligible as the mass of the nucleus is more than three orders of magnitude larger than that of the electron.

At the high-energy end of the energy spectrum, pair production has the highest cross section. During this process an electron-positron pair is created. An energy of $E_\gamma \geq 2 \times 511$ keV is required for pair production to be able to take place at all, where 511 keV is the rest mass of an electron. Through this process the γ-ray disappears completely, and the energy exceeding 1.022 MeV goes into kinetic energy of the electron-positron pair.

The electrons and positrons produced via pair production have a relatively short mean free path, and are usually stopped completely after a very short distance in matter. Once slowed down, the positron annihilates with an electron in the medium, which typically produces two back-to-back 511 keV γ-rays.

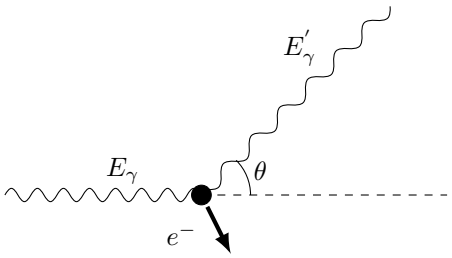

Figure 2.2: Illustration of Compton scattering. The angle θ is the scattering angle, E_γ and E_γ' are the energies of the incident and scattered γ-ray, respectively.

Compton scattering is another process in which a γ-ray interacts with an electron. It is the dominant process at γ-ray energies in the order of a few hundred keV to a few MeV. During the interaction the γ-ray transfers some of its energy to an electron. The process is illustrated in figure 2.2.

By considering the conservation of both energy and linear momentum, it is possible to relate the scattering angle to the initial and final energy of the γ-ray:

$$E_\gamma' = \frac{E_\gamma}{1 + \frac{E_\gamma}{m_e c^2}(1 - \cos\theta)} \ . \tag{2.1}$$

Here, m_e denotes the rest mass of an electron. The other symbols are defined in figure 2.2.

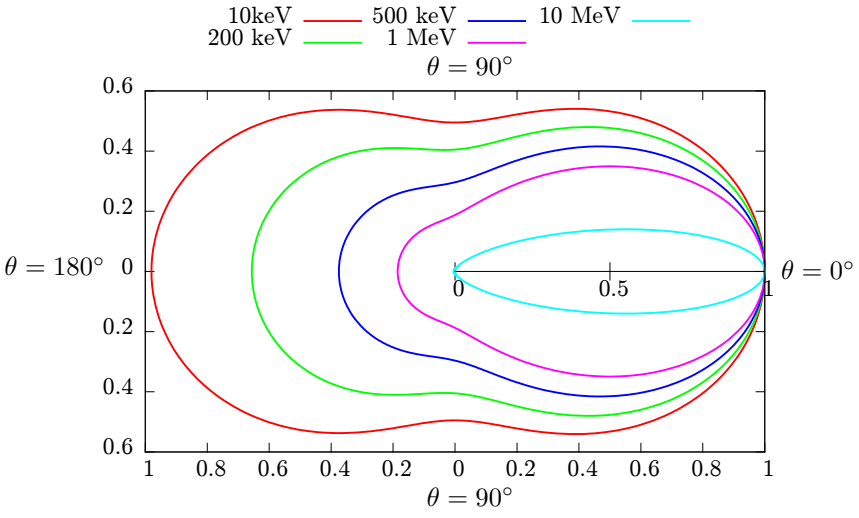

Figure 2.3: Angular distribution of Compton scattered γ-rays at different incident energies. The distance from the origin represents the cross section for the corresponding scattering angle, normalised such that it is one for $\theta = 0$.

Since the γ-ray can be scattered at any angle, the energy loss can range from a very small amount to a large fraction of the γ-ray's total energy. The angular distribution of Compton scattered γ-rays is described by the Klein-Nishina formula [1]:

$$\frac{d\sigma}{d\Omega} = \frac{r_e^2}{2} \frac{1}{(1+\alpha(1-cos\theta))^2} \left(1 + cos^2\theta + \frac{\alpha^2(1-cos\theta)^2}{1+\alpha(1-cos\theta)}\right) \tag{2.2}$$

where r_e is the classical radius of the electron, and $\alpha \equiv E_\gamma / m_e c^2$.

A graphical representation of the differential cross sections for different scattering angles, and γ-ray energies is given in figure 2.3. It is clear that small scattering angles dominate at high energies. One can also see that the distribution becomes more symmetric as the γ-ray energy decreases.

2.2 Scintillating Materials

A scintillating material produces a large amount of optical photons when subjected to ionising radiation. When energy is deposited in the material some of the energy is transferred into excitation of the atoms. This is followed by atomic deexcitations, during which optical photons are emitted. In most scintillators, and above a certain threshold, the number of scintillation photons produced is directly proportional to the amount of energy deposited in the material.

Combining scintillating materials with instruments sensitive to optical photons, for example photomultiplier tubes (PMT), is widely used as a method to detect ionising radiation [1]. In order for this method to be successful, the scintillating material must be transparent to the photons it emits. The typically linear relationship between energy deposited and number of photons also makes these detectors good at determining the energy of the incident particle.

Caesium iodide (CsI) is an inorganic crystal scintillator which is typically doped in order to achieve the desired properties. Two examples of this are CsI(Tl) and CsI(Na), whose properties are given in table 2.1. These scintillators have a very high light yield, with CsI(Tl) producing one of the largest number of photons, per keV deposited in it, of known scintillators [3]. The wavelength of the emitted light, shown in figure 2.4a, and decay times of the two scintillators

Table 2.1: Properties of CsI(Tl) and CsI(Na) which are relevant for the simulation [3].

Material	**Light yield [photons/keV]**	**Density [g/cm^3]**	**Wavelength of emission max [nm]**	**Refractive index at emission max**
CsI(Tl)	54	4.51	550	1.79
CsI(Na)	41	4.51	420	1.84

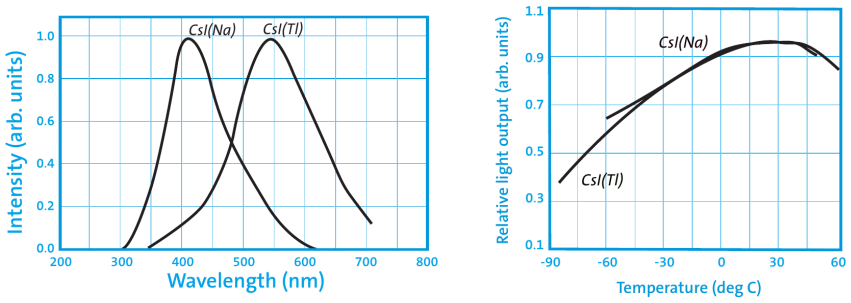

(a) (b)

Figure 2.4: (a) Intensity of emitted light of CsI(Na) and CsI(Tl) at different wavelengths, with the wavelength being inversely proportional to the photon energy. (b) Relative light yield as a function of temperature [3].

differ. They are typical properties which depend on the kind and amount of doping.

The light yield is also temperature dependent, as seen in figure 2.4b. This is important to take into account if they are to be used under non-room temperature conditions.

2.3 Electro-Optical Sensors

PMTs are a class of electro-optical sensors, commonly used in combination with scintillating materials. Electro-optical sensors produce an electrical pulse when exposed to optical photons. The first component of a PMT is a photocathode, which ejects electrons due to the photoelectric effect, when hit by optical photons. The ejected electrons are accelerated towards so-called dynodes by an electric field. When a dynode gets hit by such an electron, several additional electrons are ejected. These are then accelerated towards the next dynode, due to successively lower potential at each dynode. All of the above mentioned components are enclosed in high vacuum in order for this multiplication process to work properly.

The PMT produces an electrical pulse high enough so it can be processed by electronic equipment. The magnitude of this pulse is linearly dependent on the number of photons that hit the photocathode. Thus, when coupled with a scintillator, the produced electrical pulse is generally proportional to the energy deposited in the scintillating material.

Silicon photomultipliers (SiPM) are semiconductor detectors, consisting of an array of avalanche photodiodes. A reverse bias is applied over the photodiodes in order to create a large depleted region. When an incident optical photon deposits energy in the depleted region of the photodiode, an electron is excited into the conduction band, creating an electron-hole pair. With a sufficient reverse bias, the electron is accelerated enough to create secondary electron-hole

pairs. This causes an avalanche effect, known as a breakdown of the diode, resulting in the diode becoming temporarily conductive.

Through a very different process than PMTs, SiPMs also create an electrical pulse which can be analysed. As in the case of PMTs, the electrical pulse a SiPM creates is also proportional to the number of incident photons. This makes readout of deposited energy possible when coupled to a scintillating material. The advantage of SiPMs over PMTs is that they are comparatively very thin and compact. Thus, allowing them to be placed on all sides of a scintillator bar without noticeably interfering with incident γ-rays.

2.4 The Setup

In order to perform Compton imaging, the position of two or more points where the γ-ray interacted have to be identified. The final interaction also has to be a full absorption of the remaining γ-ray in order to determine the total energy of the incident γ-ray. The detector setup thus has to be constructed in a way such that this information can be extracted from it.

A total of six scintillator bars of dimensions $20 \times 20 \times 100$ mm^3 are positioned in two layers. In each layer three bars are placed parallel to one another, with a 20 mm spacing in between. The second layer is placed 20 mm behind the first layer, and is rotated 90 degrees with respect to the first one. It is intended to achieve one or two Compton scattering events in these two layers.

In order to extract the interaction position, and the energy deposited in the scintillator bars either PMTs or SiPMs are to be used. The PMTs have a circular sensitive area with a diameter of 8 mm, while the SiPMs have a square shaped sensitive area of 3×3 mm^2.

Due to their overall physical size, the only reasonable option for the PMTs is to place one on each end of the scintillator bars. The energy difference detected in the two PMTs can then be used to estimate the interaction position along the scintillator bar. In the case of SiPMs various setups with more than two SiPMs are conceivable. A few options, which are thought to give significantly different results, are tested in section 4, in order to determine which kind of placement provides the best position resolution.

20 mm behind the two layers of scintillator bars, a 5×5 array of scintillator detectors is placed. These scintillators have a surface of $19.5 \times 19.5\,\text{mm}^2$ each, and are 40 mm thick. The last 7 mm of the depth is inclined inwards in order to guide the photons into a photodiode placed in the back. This results in the back side being $11 \times 11\,\text{mm}^2$ [4]. This array of scintillator detectors cover an area of $100 \times 100\,\text{mm}^2$. The purpose of these are to fully absorb the γ-ray. Their physical position in space is used to estimate the position of the interaction.

Each scintillator crystal will be covered in a thin enhanced specular reflector (ESR), VM2000, which will reflect most of the photons reaching the surface of the scintillator crystals. This is done to prevent the detectors from disturbing each other, and also to increase the number of photons that reach the photocathodes.

2.5 Monte-Carlo Methods

Monte-Carlo is a broad class of numerical mathematical methods. As most numerical methods, Monte-Carlo methods' effectiveness and usability has been greatly improved with the development of modern computers. Characteristic for Monte-Carlo methods is to repeatedly calculating the result of similar events. These events typically have some randomised initial conditions or probabilistic processes. These simulations provide a distribution of possible outcomes [5].

The result of a Monte-Carlo simulation is a synthetic or virtual data set, which can be analysed. This can be used for determining the accuracy of experimental data where the uncertainties of individual measurements are known. Another application is to couple several events, whose individual behaviour is well known, in order to estimate how the sequence of events will behave.

Due to the probabilistic nature of Monte-Carlo methods, the results have an associated uncertainty. Being able to quantifying the uncertainty allows for e.g. determining the position resolution of detectors.

2.6 The `Geant4` Toolkit

The simulations in this project have been done using Geant4 [6], which is a powerful and customiseable simulation-toolkit written in the programming language C++ [7]. It provides a framework for performing Monte-Carlo simulations of interaction of radiation with matter, as well as convenient methods for creating a virtual space with complex geometries. It also contains numerous numerical approximations for physical processes and properties for a large number of materials.

Geant was initially developed for simulating detectors and high energy physics. It has since been continuously extended, and used in numerous areas within science. However for the low energy optical photons, some non standard processes still need to be activated, and optical properties of materials need to be defined by the user. These features are turned off by default as the large number of optical photons that can be produced is very computationally intensive.

Geant4 also provides several built-in methods for writing data to files. The available output formats are CSV, ROOT, XML, and HBOOK.

3 Simulations with Geant4

In order to get a Geant4 [6] application running there are several classes which must be implemented in the correct way to synergize with each other. To start such a project from scratch would be a time consuming and inefficient task for anyone not familiar with the structure. Therefore, an example where optical photons and the scintillation process were already activated, was used as a starting point of the simulations described in this section. All these simulations were performed using version 10.0.2 of Geant4.

The example, called OpNovice, already contained all files required for a simple, but functional, simulation with scintillation processes. The geometries, materials and their optical properties were modified to match the specific needs of this project. Further, a format for writing data to output files was created, in order to analyse the produced data sets.

3.1 Geometries

For the purposes of the present simulation a rather limited number of geometries was required, as the setup features many replicas of a small set of them. Both

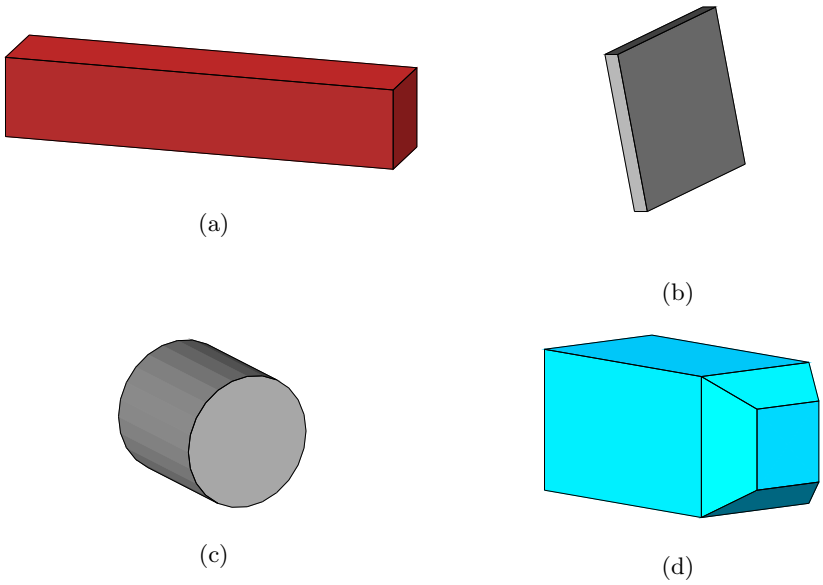

Figure 3.1: (a) The shape of the scintillator bars, made from a Geant4 box. (b) Another box shape, used for the SiPMs. (c) The cylindrical shape of the PMTs. (d) The polyhedral shape of the scintillator elements in the wall. Figures not to scale. The dimensions of the geometries are described in section 2.4.

the scintillator bars and the SiPMs are simple boxes shown in figure 3.1a and 3.1b. The PMTs were simulated as solid carbon cylinders as shown in figure 3.1c. The inner components were not simulated as that is beyond the scope of this project. The PMTs are simulated to add the possibility of realistic noise from γ-ray scattering in the PMT before interacting in a scintillating volume.

Figure 3.1d shows the shape of the scintillator crystals which make up the so-called wall, which can be seen in figure 3.3. This is an example of a geometry generated by the polyhedra method.

3.2 Geometry of the Detector Setup

In order to quickly replicate an entire assembly of volumes, all elements which constitute the detector are assembled into one entity. Behind each PMT and SiPM a very thin volume, which is made sensitive to optical photons, is placed. This can be seen in figures 3.2c and 3.2d. These sensitive elements are described in more detail in section 3.5.

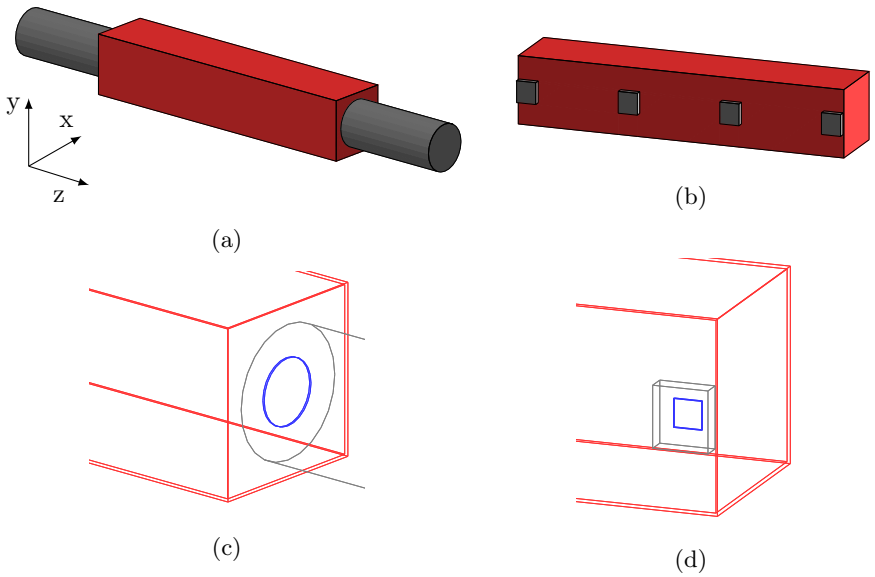

Figure 3.2: The red boxes are scintillator bars. (a) Grey cylinders are PMTs. (b) Grey squares are SiPMs. (c)(d) Blue elements are made sensitive to optical photons, and are placed such that they touch the scintillator bar. The layer between the two red volumes represents the ESR, VM2000.

The volume which represents the scintillator crystal is placed inside a slightly larger volume. This creates a thin layer covering the entire scintillator, with the purpose of replicating the thin light-reflecting ESR, VM2000, which covers the scintillator crystal. This thin layer can be seen in figures 3.2c and 3.2d.

The entire setup can be constructed by creating several instances of the already defined detector elements. The complete setup with PMTs employed is shown in figure 3.3. The scintillator bars are shown in red with the grey cylinders in the ends representing the PMTs. The wall is shown in blue, where the individual elements are visible.

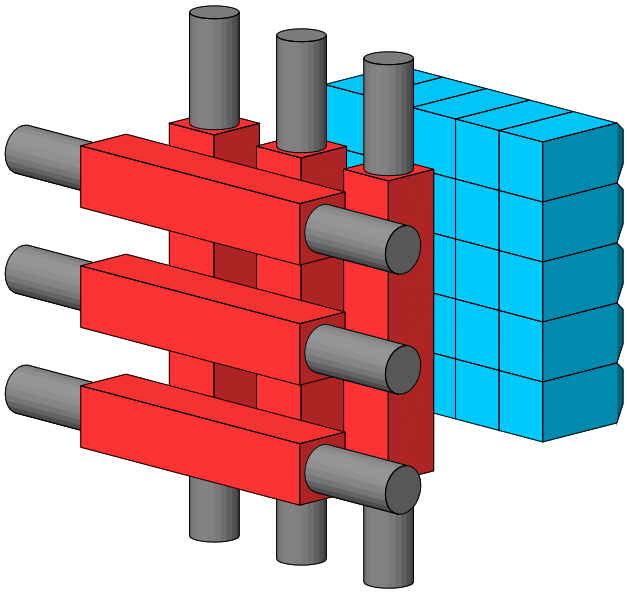

Figure 3.3: Entire detector setup using PMTs attached to the scintillator bars. The wall of scintillator elements is shown in blue. The red boxes are the scintillator bars, and the grey cylinders are the PMTs.

3.3 Materials

As particles interact with different cross sections depending on the material in which they travel, the material for each volume has to be defined. Geant4 has a large number of predefined materials which can be used. As for any material not in Geant4's predefined database, compounds can be defined using any combination of elements and isotopes, with user-defined density and ratio between the different components.

The volumes included in the simulation are listed with their respective materials in table 3.1. All materials except for caesium iodide and ceramic were retrieved from the database. These compounds were defined manually as an academic exercise. Caesium iodide was defined as a compound with a one to one ratio of caesium and iodine, and a density of 4.51 g/cm^3. For the ceramic material aluminium oxide (Al_2O_3) was used, with a density of 3.97 g/cm^3.

Table 3.1: Materials assigned to each virtual volume.

Volume:	**Material:**
Scintillator crystals	Caesium iodide
PMTs	Carbon
Sensitive volume in PMTs	Carbon
SiPMs	Ceramic
Sensitive volume in SiPMs	Silicon
Foil covering the scintillators	Aluminium
World volume	Air

The caesium iodide in the scintillator bars is doped with either sodium or thallium. As the fraction of doping atoms is very low, it is assumed to not affect the cross section for γ-ray interactions. The type of doping is thus ignored when constructing and assigning the compound. However, the type of doping does affect the scintillating properties significantly. This is accounted for by specific scintillation properties assigned to the compound (see section 3.4).

3.4 Physics Processes

The example, which was used as a starting point, uses a user-defined physics list, where individual physics processes are added to the process manager. Relevant processes have to be added for each particle type. Table3.2 shows the processes for γ-rays, electrons and positrons. There exist many different ways to numerically approximate how these particles interact with matter. However for this work, the so-called standard library was used.

Table 3.2: Processes which are applicable to γ-rays, electrons and positrons.

Particle:	**γ-ray**	**Electron**	**Positron**
Processes:	Photoelectric effect Compton scattering Pair production	Multiple scattering Ionisation Bremsstrahlung	Multiple scattering Ionisation Bremsstrahlung Annihilation

Additionally to the processes shown in table 3.2, a scintillation process and a Cherenkov process is applied. These are applied to a subset of all the particles, as not all of them produces scintillation and Cherenkov photons. For example, the γ-ray doesn't produce any scintillation photons. They are produced by secondary electrons.

For optical photons the following processes are added:

- Absorption
- Rayleigh scattering
- Mie scattering
- Reflection and refraction processes

The absorption process requires an absorption length for the material in which the optical photon is moving. The used absorption lengths are shown in table 3.3. An absorption length of zero is used for aluminium, silicon and carbon as these materials are completely opaque to optical photons. Other materials do not need properties for optical processes as no optical photons will be able to reach them.

Properties for the scintillation process must be added explicitly to the *material properties table* of the scintillating material. The parameters which define the scintillation spectrum for CsI(Na) are given in table 3.4. The total scintillation yields given in table 2.1 are used in the simulations. The scintillation yield as a function of time is disregarded, as using timing for determining positions requires a full simulation of the readout electronics, which is beyond the scope of this project.

Table 3.3: Optical properties for materials which come in contact with optical photons. For carbon and silicon the same refractive index as the one used for CsI is applied.

Material:	**CsI(Na)**	**CsI(Tl)**	**Carbon**	**Silicon**	**Aluminium**
Absorption length [cm]:	33	33	0	0	0
Refractive index:	1.84	1.79	1.84/1.79	1.84/1.79	1.00

The employed materials also need a refractive index in order for optical photons to be able to propagate in them. It is also important for the boundary processes. The refractive indices are given in table 3.3. Caesium iodide is given the refractive index which corresponds to the wavelength at its emission maximum. This is of course not exactly true for the entire emission spectrum, but it is a sufficient approximation. Slightly different refractive indices are not expected to affect the outcome of the simulation significantly.

Carbon and silicon are given the same refractive index as the one currently used for CsI to emulate the glue which keeps the detector in place. This glue is designed to have the same refractive index as the crystal in order to let as many photons as possible hit the electro-optical sensor. In reality it is not exactly the same, which will make the simulated detector slightly more efficient than the real one.

Table 3.4: Parameters which define the scintillation spectra of CsI(Na) in the simulation. The photon yield is normalised to the yield at the emission maximum. The values are extracted from figure 2.4a [8].

Photon energy [eV]	**Photon yield [arb.]**
3.8149	0.068
3.5424	0.264
3.30624	0.566
3.0996	0.949
2.91727	0.940
2.7552	0.732
2.61019	0.523
2.47968	0.387
2.3616	0.260
2.25426	0.149
2.15625	0.068
2.0664	0.021

As the foil is designed to reflect as many optical photons as possible, perfect reflectivity is assumed. A dielectric, polished metal surface is defined. This surface is then applied to the aluminium volume using a skin surface. This causes any photon which tries to enter the aluminium to be reflected. Because of this the refractive index for aluminium is not important, and is set to one.

3.5 Recording Data

For each type of volume, which is desired to be sensitive, a sensitive detector class was created, instantiated and attached to the volume type. Whenever an optical photon enters the sensitive part of either a PMT or a SiPM it has a certain, energy-dependent, probability of being counted as detected. This is done in order to account for the quantum efficiency of the electro-optical sensors. The quantum efficiency profile of the PMT, and the approximation used in the simulation is shown in figure 3.4a. Corresponding profiles for the SiPMs are shown in figure 3.4b.

If an optical photon is detected by an electro-optical sensor, a hit object is created and sent to the hits collection. A hit object stores an identification number (ID) of the detector, the energy of the optical photon, and the time at which it was detected inside the volume. Subsequently to obtaining this information, the optical photon track is killed as its information has been accounted for.

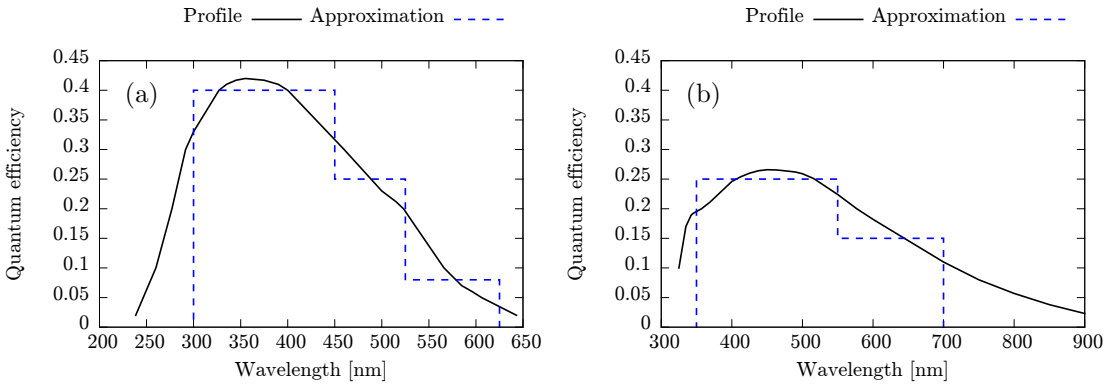

Figure 3.4: The black lines show the quantum efficiency profile, and the blue, dashed lines show the approximations used for the quantum efficiencies in the simulations. (a) PMT Hamamatsu R9880U-210 [9]. (b) SiPM Hamamatsu S12572-015C [10].

The scintillator crystals themselves were also made sensitive in order to store exact interaction points, and energy deposition by the incident γ-ray. These sensitive detectors thus only generate hits if the detected particle is the primary particle, and it deposited energy. The hits generated in these cases store the ID of the scintillator crystal, the energy lost, the current time, as well as the three-dimensional position.

At the end of each event the number of photons detected in each PMT and SiPM is summed up, and written in listmode to a file, together with the detector ID and the time of the first photon detected. All the non-optical information, described in the previous paragraph, from the scintillator hits is also written to the same files.

The used output format is ASCII-files, chosen for their simplicity and ease of use. The simulation utilises the multithreaded capabilities of Geant4. Thus, one output ASCII file is written for each of the threads.

4 Position Resolution in the Scintillator Bars

Simulations with a single scintillator bar were performed in order to identify how to extract the position of the γ-ray interaction. Four different configurations of electro-optical sensors were tested. 100 000 events, with one incident 511 keV γ-ray per event, were simulated. Approximately 50 000 interactions were recorded for each configuration, as many of the γ-rays went through the scintillator bar without interacting.

The position resolution of the different configurations is evaluated in this section by comparing the number of photons collected in the electro-optical sensors to the, in the simulation, known interaction position. The axes used for all setups are defined in figure 3.2a, and the origin is defined to be at the centre of the scintillator bar.

4.1 Photomultiplier Tubes

The configuration with PMTs is shown in figure 3.2a. The difference between the number of photons in each PMT, normalised by the total number of photons detected, was used as an indication of the z-position:

$$z = \frac{N_1 - N_2}{N_{tot}} \tag{4.1}$$

Here N_1 and N_2 denote the number of photons detected in each PMT, and N_{tot} is the total number of photons detected in both PMTs. This value is plotted against the known interaction position, extracted in the simulation, in figure 4.1a.

The least square method is used to fit a straight correlation line through the data. If the weighted mean interaction z-position, z_i, is not within the interval $-40 < z_i < 40$ mm, the point is ignored for the linear fit since the resolution clearly becomes very bad near the ends of the bar.

The bad resolution for $z_i > 40$ mm and $z_i < -40$ mm, seen in figure 4.1a, is attributed to the fact that the PMT does not cover the entire side of the scintillator bar. If an interaction takes place directly in front of the PMT it will collect an abnormally large amount of photons. This causes the large number of entries above the correlation line near $z_i = 50$ mm, and the similar entries below the correlation line near $z_i = -50$ mm. However, if the interaction takes place near the end but in a corner, a large amount of photons will be reflected in the aluminium foil. Thus, the PMT at the other end will collect an unexpectedly large amount of photons. This causes the somewhat smaller deviation from the correlation line above it near $z_i = -50$ mm and below it near $z_i = 50$ mm.

The line shown in figure 4.1a serves as a calibration line for the position measurements. If the calibrated measured position was outside of the scintillator bar it was discarded at this point. An attempt to keep these points was made by assuming that the interaction took place at, or near, 50 mm if the measured position was above 50 mm, and at, or near, -50 mm if the measured position was below -50 mm. However, this introduced significantly larger measurement

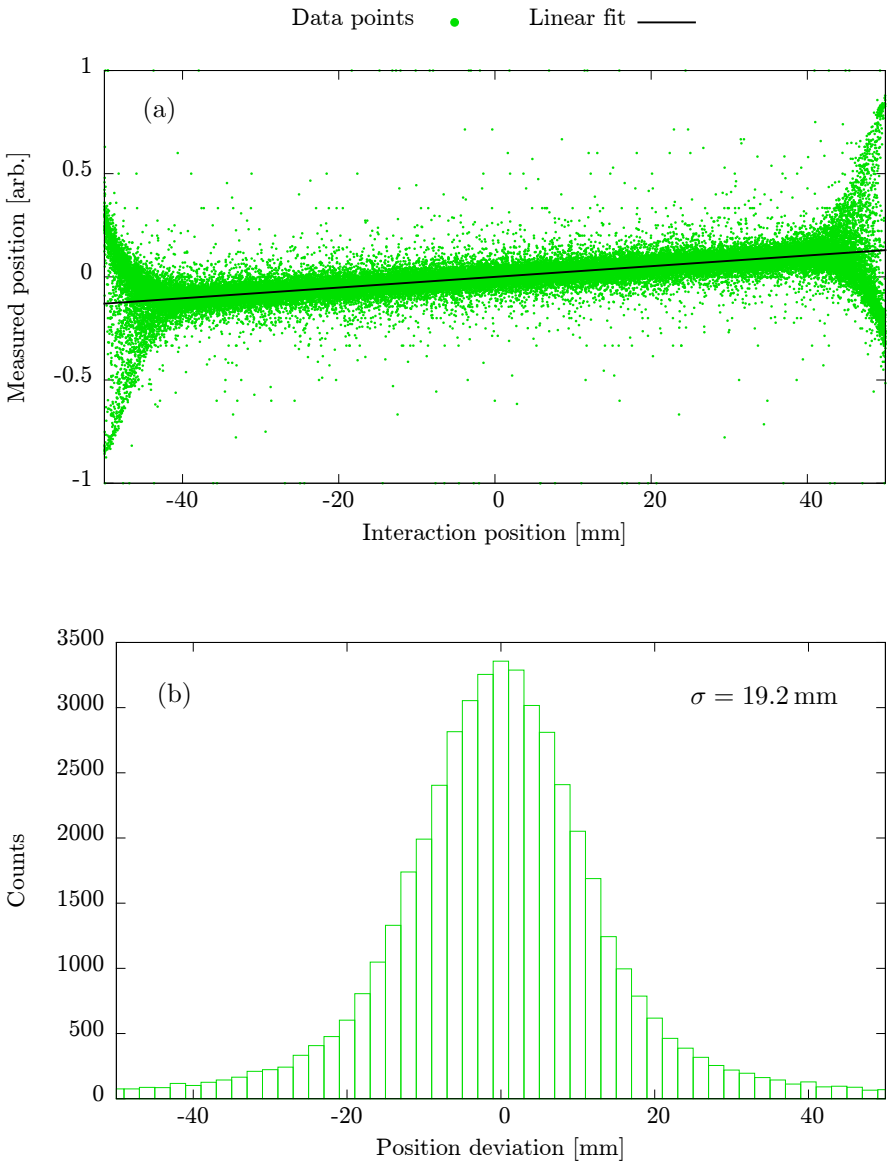

Figure 4.1: (a) The y-axis shows the difference in number of photons collected in each PMT, divided by the total number of photons collected. The x-axis shows the mean interaction z-position weighted by the energy deposited. The black line was obtained by the least squares method, using the points within the interval $z_i \in [-40\text{ mm}, 40\text{ mm}]$. (b) Deviation of the measured position from the weighted mean position using the linear relationship represented by the black line in (a). Here σ is the standard deviation.

errors than just discarding these points, due to the fact that there are entries which deviates significantly from the correlation line, both above and below it, on both sides of the plot.

In order to determine the accuracy of the calibrated position measurement, the deviation from the real weighted mean z-position was calculated. The binned result is shown in figure 4.1b, along with σ, the standard deviation.

4.2 Four Silicon Photomultipliers on One Side

The configuration with four SiPMs on one side is shown in figure 3.2b. The number of photons collected in each SiPM is weighted by their physical position along the z-axis, and then normalised by the total number of photons. The positions of the SiPMs where also normalised to ± 1 and ± 3 respectively, as only their relative distances from the centre are relevant for the calibration line. Thus, the uncalibrated z-position is calculated as:

$$z = \frac{-3 \cdot N_1 - N_2 + N_3 + 3 \cdot N_4}{N_{tot}} \tag{4.2}$$

Here N_i denotes the number of photons detected in the i:th SiPM, numbered from the left in the figure.

This value is plotted against the weighted mean z-position of the interaction in figure 4.2a. A linear least squares fit is used to calculate a calibration line, also shown in this figure. In this case all points were used as no regions exist which obviously deviated from the general trend.

In figure 4.2a a number of points can be seen to line up at integer values for the measured position. This is most likely caused by very weak interactions where only a small number of optical photons were produced, and just one or two SiPM detected a non-zero amount of photons.

Just like in the case of PMTs, an attempt to keep data points with a calibrated measured position outside of the scintillator bar was made. Also in this case it introduced much larger uncertainty in the measured position. Despite the fact that there are no obvious deviations from the correlation line in figure 4.2a which would cause ambiguity in the corresponding position. Due to this, no further attempts to keep points measured to be outside the scintillator where done in the following analysis sections.

The binned data of the deviation of the calibrated, measured z-position from the weighted, mean z-position and the related standard deviation is shown in figure 4.2b. It clearly shows that this setup, with four SiPMs on one side, gives a significantly better position resolution in the z-direction compared to using two PMTs at the ends.

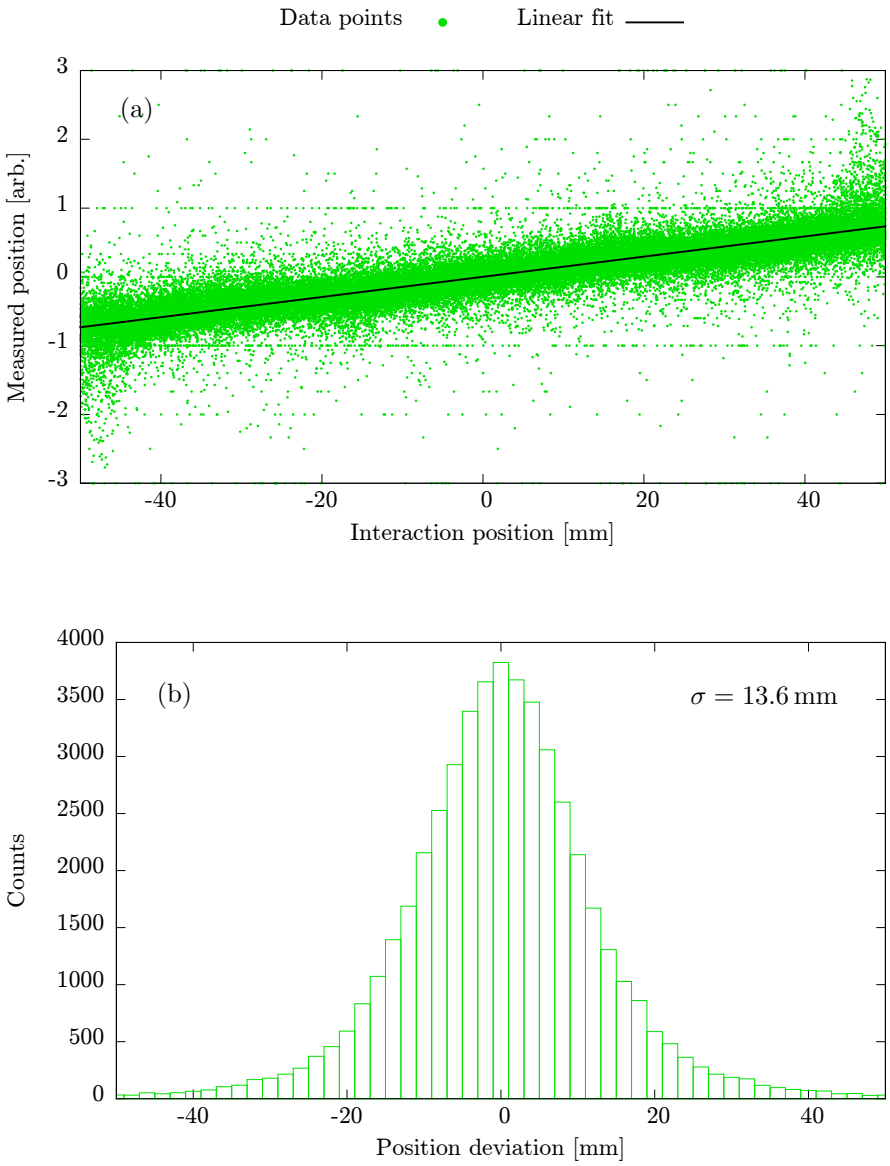

Figure 4.2: (a) The y-axis shows the number of photons in each SiPM weighted by the physical position of corresponding SiPM, normalised by the total number of photons collected. The x-axis shows the mean interaction z-position weighted by the energy deposited. The black line is the calibration line, obtained by the least squares method for a linear function. (b) Deviation of the measured z-position from the weighted mean interaction z-position. The calibration line in (a) is used to calibrate measured position. Here σ is the standard deviation.

4.3 Eight SiPMs, Four in Each End

As an attempt to improve the idea behind the PMT setup discussed in section 4.1, four SiPMs were placed on each end of the scintillator bar. This configuration is shown in figure 4.3. As the sensitive area of these four SiPMs are more spread out than the sensitive area of a single PMT, the ambiguity near the ends should be reduced.

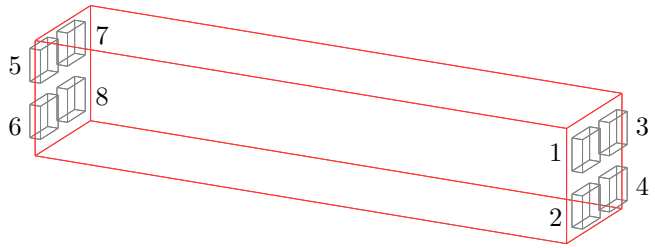

Figure 4.3: Wire frame representation of the scintillator bar. Grey boxes show the placement of the SiPMs, with the respective numbers representing their ID.

The number of photons detected in the SiPMs were summed for each end of the scintillator, and the uncalibrated z-position was calculated as:

$$z = \frac{(N_1 + N_2 + N_3 + N_4) - (N_5 + N_6 + N_7 + N_8)}{N_{tot}} \tag{4.3}$$

Figure 4.4a shows the measured z-position plotted against the weighted mean z-position of the interactions. The regions which deviate from the correlation line were indeed reduced. However, as the total sensitive area is smaller, the inclination of the correlation is smaller than for the PMTs. Even more importantly, the points are much more spread out around the calibration line, which again was obtained by the least squares method.

As can be seen in figure 4.4b, the accuracy of this configuration is worse than using two PMTs. The disadvantages of smaller sensitive area coupled with the lower quantum efficiency, seen in figure 3.4, cannot be outweighed by a more spread-out sensitive area.

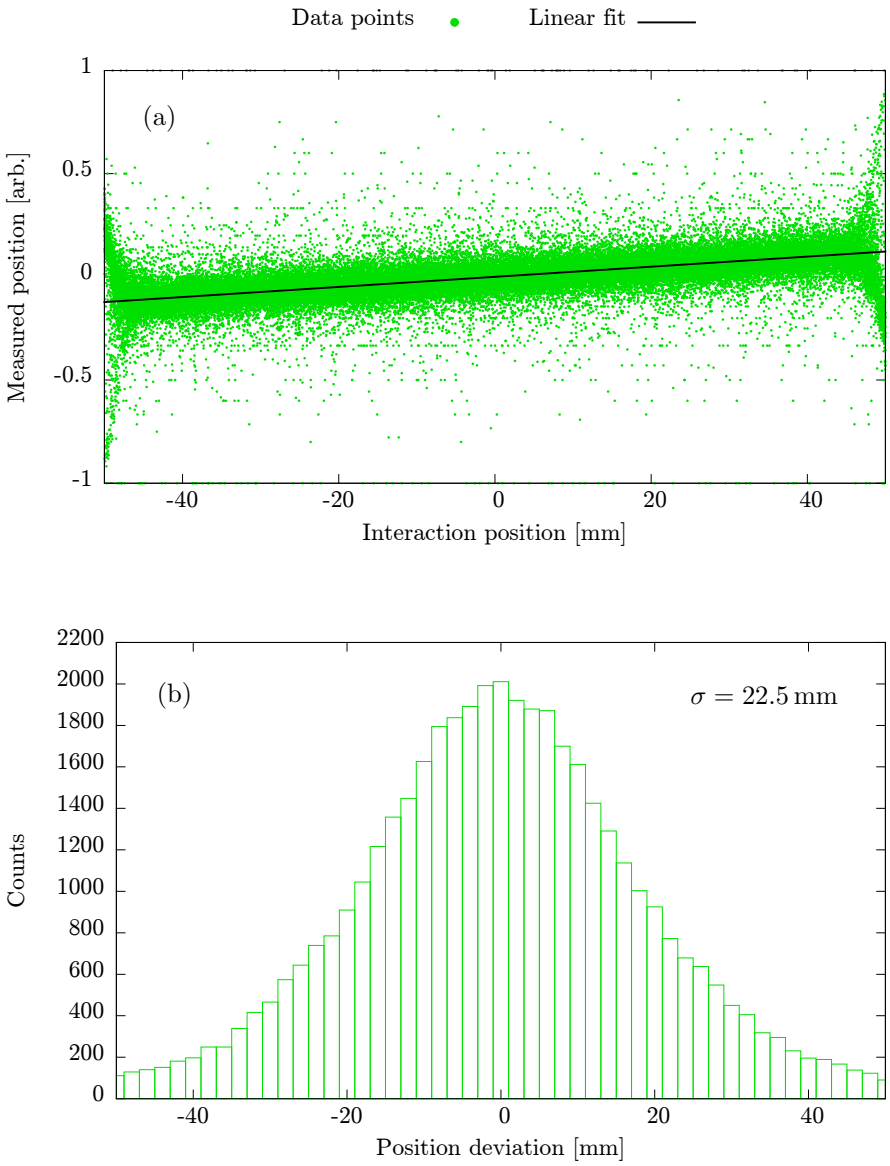

Figure 4.4: (a) The y-axis shows the number of photons in each SiPM weighted by the physical z-position of corresponding SiPM, divided by the total number of photons collected. The x-axis shows the mean interaction z-position weighted by the energy deposited. The black line was obtained by the least squares method. (b) Deviation of the measured z-position from the weighted mean z-position. The linear relationship represented by the black line in (a), is used as a calibration line for the measured position. Here σ is the standard deviation.

4.4 Eight SiPMs on the Sides

As the position resolution using SiPMs on the side gave better position resolution than placing them on the ends, another configuration with SiPMs on the sides was tested. Two SiPMs were placed on each of the four sides, one by each of the two ends, as shown in figure 4.5.

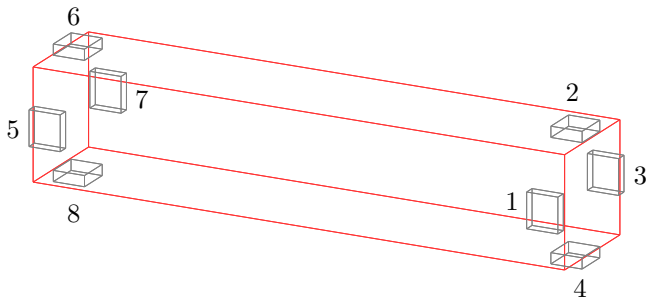

Figure 4.5: Wire frame representation of the scintillator bar. Grey boxes show the placement of the SiPMs, with the respective numbers representing their ID.

The uncalibrated z-position where calculated as:

$$z = \frac{(N_1 + N_2 + N_3 + N_4) - (N_5 + N_6 + N_7 + N_8)}{N_{tot}} \tag{4.4}$$

where N_i denotes the number of photons detected in the i:th SiPM. The result is plotted against the weighted mean interaction z-position in figure 4.6a.

The calibration line was obtained by the least squares method. The deviation of the calibrated measured z-position from the real weighted mean interaction position is shown in figure 4.6b.

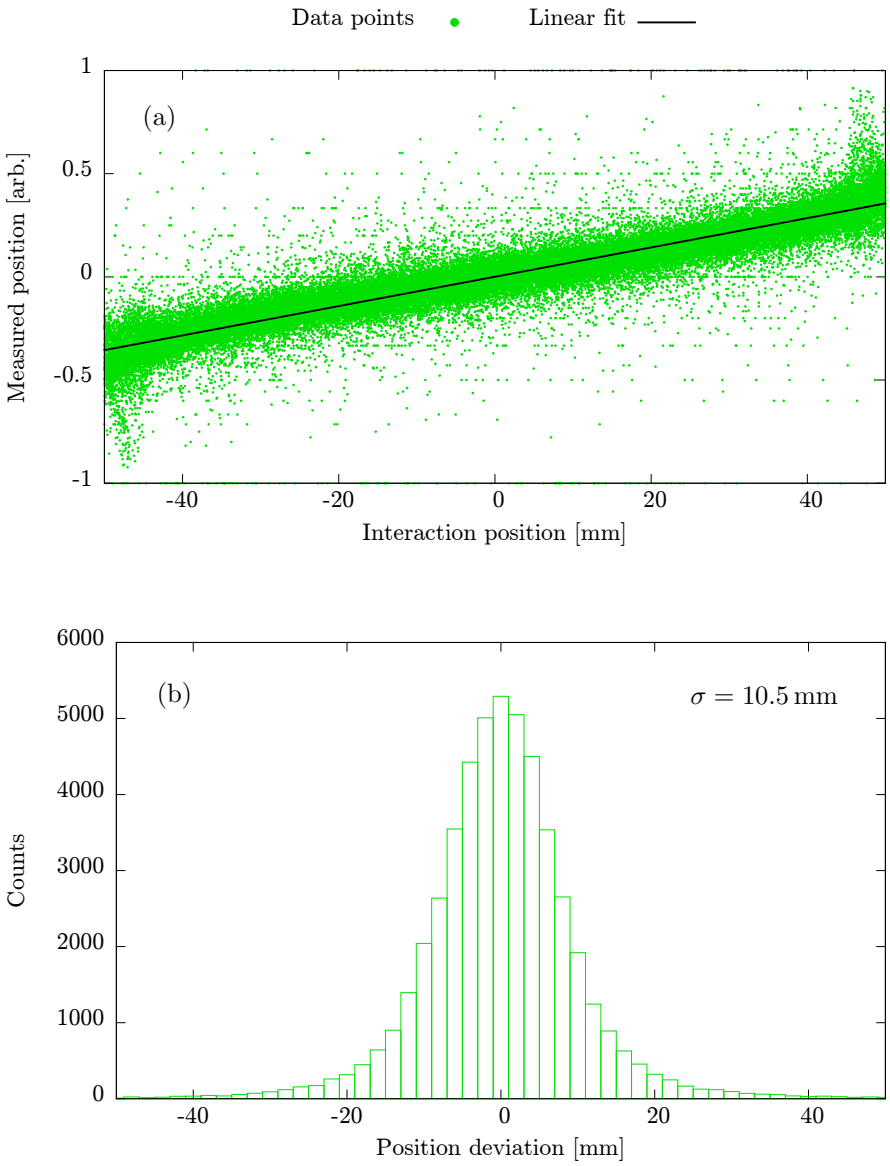

Figure 4.6: (a) The y-axis shows the number of photons in each SiPM weighted by the physical position of the SiPM, divided by the total number of photons collected. The x-axis shows the mean interaction position weighted by the energy deposited. The black line was obtained by the least squares method. (b) Deviation of the measured position from the weighted mean position. The linear relationship represented by the black line in (a), is used as a calibration line for the measured position. Here σ is the standard deviation.

4.5 Further Analysis of Two Configurations

In this section the possibility to improve the position resolution by discarding certain data points was investigated. The configuration with two PMTs shown in figure 3.2a, and the configuration with eight SiPMs shown in figure 4.5, were chosen for further analysis.

The total number of photons detected in the respective kind of electro-optical sensors where counted for each event. The number of events as a function of the number of photons detected are plotted in figure 4.7a for the PMT configuration, and in figure 4.7b for the SiPM configuration. The Compton spectrum and the full absorption peak is visible in both spectra. The full absorption peak is slightly extended towards higher photon counts. This is attributed to statistical variations of the number of photons detected in the electro-optical sensors. The number of photons detected in the two PMTs is significantly larger than that of the eight SiPMs. This is expected as the PMTs have both a larger total surface area and a higher quantum efficiency.

In order to improve the accuracy of the configuration with PMTs, points with a mean weighted interaction position larger than 40 mm or smaller than -40 mm were ignored for the calculation of the position resolution. This effect could be achieved practically by e.g. placing a block of lead in front of these regions. This significantly improved the position resolution, and the standard deviation was reduced by approximately 30%. Additionally, a threshold on the number of photons was employed in order to ignore interactions with very little statistics. Ignoring points with less than 300 detected photons in a single event removed the majority of the points far away from the correlation line, which is visible in figure 4.1a. The corresponding plot with the threshold employed is shown in figure 4.7c. The threshold further improved the accuracy, reducing the standard deviation to 11.1 mm which can be seen in figure 4.7e.

A similar threshold at a total of 150 photons per event were employed for the configuration with SiPMs. Also in this case the threshold removed the majority of the points far away from the correlation line, which can be seen in figure 4.5. This includes the vertical lines of points, visible for all three configurations with SiPMs discussed in sections 4.2-4.4. With this threshold the accuracy was improved noticeably as can be seen in figure 4.7f, yielding a standard deviation of 7.4 mm.

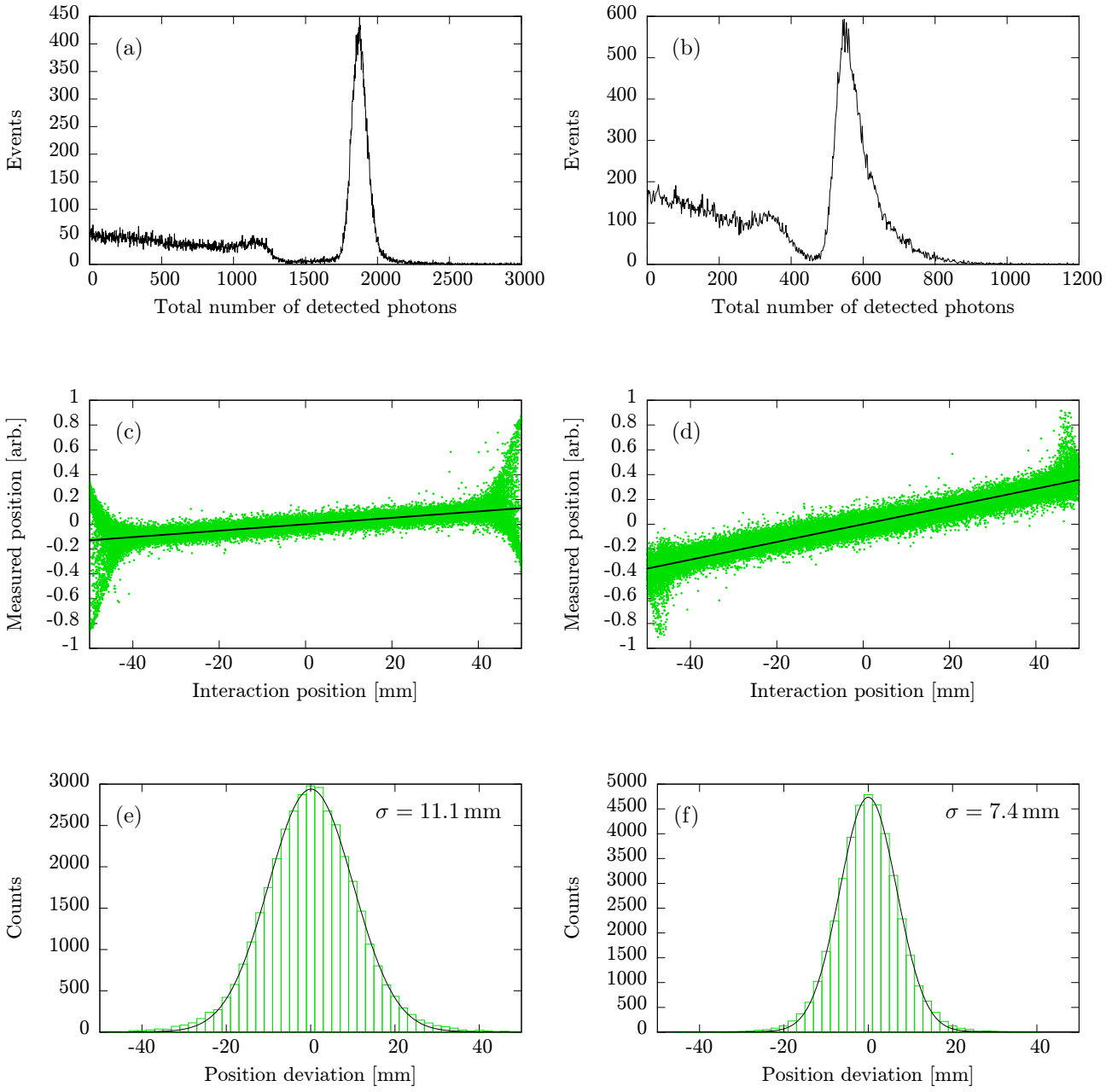

Figure 4.7: All the figures on the left refer to the configuration with two PMTs shown in figure 3.2a, and all the once on the right refer the the configuration with eight SiPMs shown in figure 4.5. (a) and (b): Frequency of events as a function of total number of photons detected. (c) and (d): Uncalibrated z-position as a function of the mean weighted interaction position, with a threshold. Black lines are calculated by the least squares method. (e) and (f): Deviation of the calibrated z-position from the mean weighted interaction position, with standard deviation σ. Black lines are Gaussian functions with flat background calculated with the least squares method.

4.6 Position in the x-y Plane

As the γ-rays are generated by a uniform distribution from one side of the scintillator bar, they are also expected to enter the scintillator bar with a uniform distribution. However, the mean interaction position weighted by the energy deposition, which is what will be measured, will not be quite uniformly distributed. Multiple interactions make it very unlikely to obtain a mean interaction near the top and bottom of the scintillator bar. This effect can be seen in figure 4.8a.

The border effects should affect points near the top and the bottom equally, and the distribution is thus expected to be symmetric around zero. The fluctuations in the data, and the non-zero mean is therefore interpreted as an indication of a rather small sample size. The standard deviation is somewhat smaller than that of a uniform distribution with the same bounds, which is to be expected.

The initial interaction position along the depth of the scintillator is expected to follow an exponential attenuation, as the probability for the γ-ray to interact is constant throughout the scintillator material. However, due to the same border effects discussed above, the weighted mean interaction position is expected to be shifted away from the edges. This can be seen in figure 4.8b.

The mean value is smaller than one, which is what would be expected for a distribution which somewhat resembles an exponential attenuation. The standard deviation is also in this case smaller than that of a uniform distribution, which also is expected.

Just using the physical position of the scintillator bar as an estimate of the position in the x-y plane yields a significantly better position resolution than that along the z-axis of even the most accurate configuration.

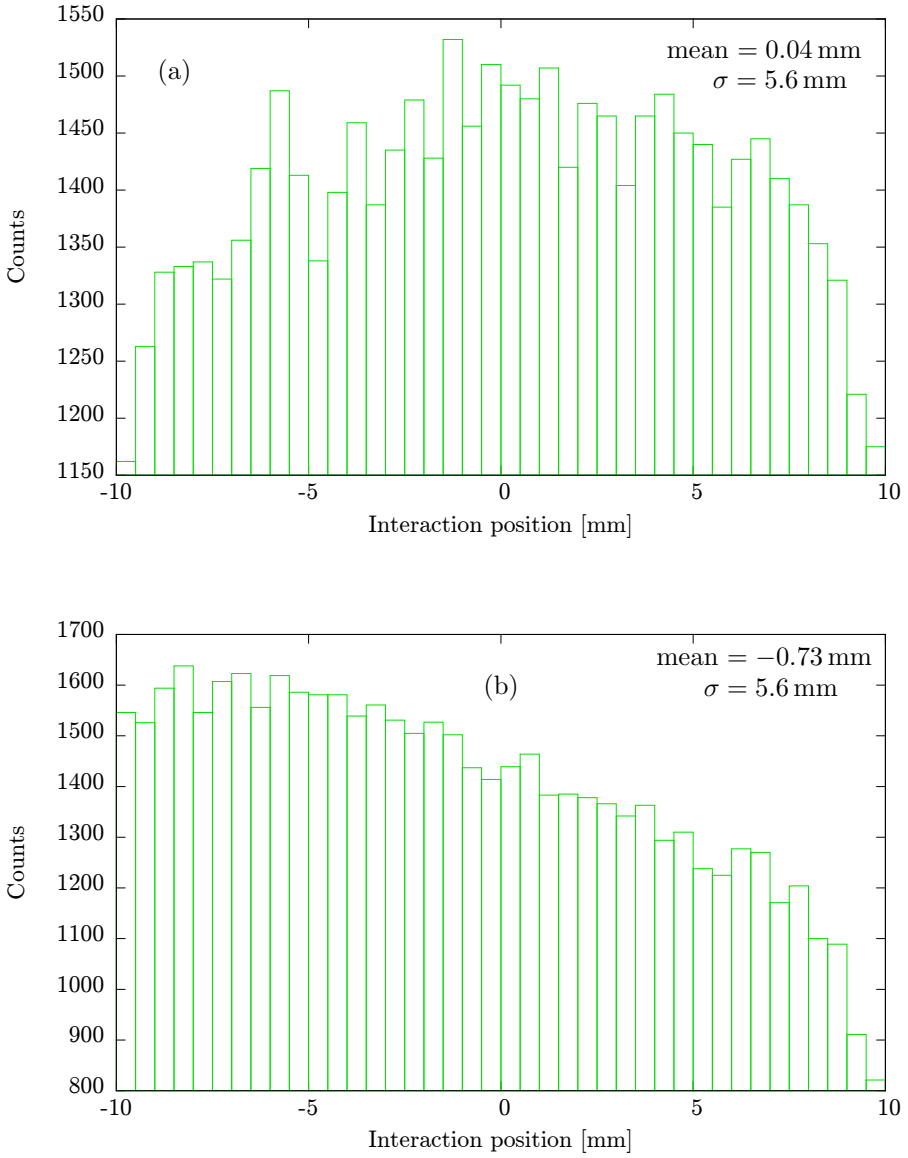

Figure 4.8: (a) Binned weighted mean interaction position along the height, or the y-axis in figure 3.2a, of the scintillator bar. (b) Binned weighted mean interaction positions along the depth, or the x-axis in figure 3.2a, of the scintillator bar. Here σ are the standard deviations.

5 Imaging Algorithm

For determining the origin of γ-rays, the first step is to identify the number of interactions in a single event. At least two interaction positions are required. The first one should be a Compton scattering event, in order to determine an incident angle [11]. Additionally, the energy that the γ-ray deposited at each of the interaction points needs to be identified.

In order to identifiy the initial interaction point of the γ-ray, a combination of timing and energy deposition is used. The Klein-Nishina formula, given in equation 2.2, is used to relate the deposited energy to which interaction point is most likely to have been the first one. This is coupled with the timing of the readouts in order to better estimate this likelihood.

When the initial interaction point has been identified, equation 2.1 can be used to calculate the scattering angle. This allows to project a cone in three-dimensional space with possible origins of the γ-ray, as seen in figure 5.1.

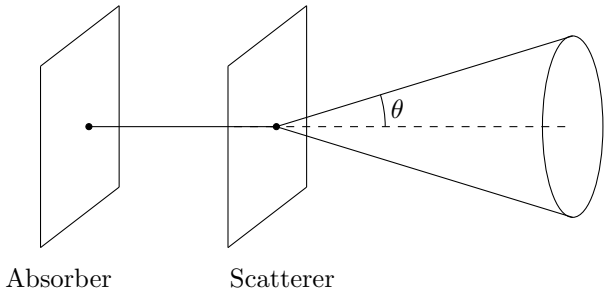

Figure 5.1: Schematic showing how the cone is projected in space, given two interaction points and the related scattering angle. The absorber represents the wall, shown in figure 3.3, and the scatterer could represent either of the two layers of scintillator bars in the same figure.

To construct the image of the source, a two-dimensional histogram in the angular plane can be used. Each tracked γ-ray yields a circle in this plane. The center of this circle is given by the vector between the first and the second interaction points, and the radius of the circle is determined by the related scattering angle. The position of the source could then be estimated by counting the number of circles which intersects each bin, as most circles are expected to intersect at the origin of the γ-rays.

6 Summary and Outlook

Simulations of a single scintillator bar with a few different configurations of electro-optical sensors have been performed. Position accuracies along the scintillator bar down to approximately 8 mm, corresponding to 8% of the scintillator bar's length, have been deduced from these simulations. A functioning Geant4

application for performing these simulations has been created, which can be used to simulate similar configurations and setups with very little additional effort.

For the individual scintillator bars, simulating the configuration with two PMTs with the addition of lead blocks placed in front of the ends, as suggested in section 4.5, would be interesting. This passive shielding has a potential to significantly improve the position resolution of the configuration with PMTs.

Many more configurations with SiPMs are conceivable, which might yield a better position resolution. For example, not placing all eight SiPMs in the very end of the scintillator bar, as the configuration in figure 4.5, could reduce the deviation of the entries near the edges in figure 4.7d. Alternatively fitting a third-degree polynomial to the same correlation might yield a better position resolution.

The thresholds discussed in section 4.5 could also be further optimised. Increasing the lower threshold further improves the position resolution, but it reduces the fraction of events which are detected. This should be optimised depending on the intensity of the source, the required resolution, and the time available for collecting data in real space.

Additionally, the number of photons detected in one side of the scintillator bar could be plotted against the number of photons detected on the other side. Such a two-dimensional plot allows for more sophisticated filters by selecting or cutting out certain regions of data points.

In this work simulations have only been performed with the sodium doped CsI(Na). CsI(Tl) is expected to yield worse position resolution as the peak in its scintillation spectrum does not match the peak in the quantum efficiency of the electro-optical sensors as nicely as that of CsI(Na). Yet it is desireable to perform simulations in order to evaluate this.

Once a satisfactory position resolution has been obtained in the scintillator bar, the next step is to employ the configuration which gave the best position resolution in the full detector setup. Then run simulations where γ-rays are generated from a specific point, with randomised direction. Simulating such events would yield data where interaction multiplicities could be identified, and imaging algorithms, discussed in section 5, can be applied. The spacial resolution for a point-like source could then be evaluated.

Further simulations of the entire setup with different γ-ray energies would be valuable for testing imaging algorithms for higher multiplicities. Finally, simulations of finite sized radioactive samples would allow for determining how accurate the detector setup can identify the shape and direction of a γ-ray source.

By physically constructing the detector, real measurements could be compared to the simulated results. This would allow for evaluating the accuracy of the simulations, as well as provide feedback on how the simulations can be improved. Being able to accuratly simulate the detector setup would not only help gaining insight into the physics behind the detectors, but it would also provide a way to self-consistently improve the experimental setup and the simulation of it.

References

[1] William R. Leo. *Tehcniques for Nuclear and Particle Physics Experiments*. Springer-Verlag, second revised edition, 1994.

[2] M.J. Berger, J.H. Hubbell, S.M. Seltzer, J. Chang, J.S. Coursey, R. Sukumar, D.S. Zucker, and K. Olsen. National Institute of Standards and Technology. Photon Cross Sections Database. `http://www.physics.nist.gov/PhysRefData/Xcom/Text/XCOM.html`, 2009. Accessed: 2014-12-1.

[3] Saint-Gobain Ceramics & Plastics, Inc. *CsI(Na), CsI(Tl) Cesium Iodide Scintillation Material*, 2007.

[4] P. Golubev et al. The Lund–York–Cologne Calorimeter (LYCCA): Concept, design and prototype developments for a FAIR-NUSTAR detector system to discriminate relativistic heavy-ion reaction products. *Nuclear Instruments and Methods in Physics Research Section A: Accelerators, Spectrometers, Detectors and Associated Equipment*, 723(0):55 – 66, 2013.

[5] Malvin H. Kalos and Paula A. Whitlock. *Monte Carlo Methods*, pages 1–5. Wiley-VCH Verlag GmbH & Co. KGaA, 2009.

[6] S. Agostinelli et al. Geant4—a simulation toolkit. *Nuclear Instruments and Methods in Physics Research Section A: Accelerators, Spectrometers, Detectors and Associated Equipment*, 506(3):250 – 303, 2003.

[7] J. Allison et al. Geant4 developments and applications. *IEEE Transactions on Nuclear Science*, 53(1):270–278, 2006.

[8] N. Lalovic. private comunication.

[9] Hamamatsu Photonics K.K. *Photomultiplier Tube R9880U Series*, 2014. `http://www.hamamatsu.com/resources/pdf/etd/R9880U_TPMH1321E.pdf`.

[10] Hamamatsu Photonics K.K. *(MPPC) Multi-Pixel Photon Counter, S12572-010, -015C/P*, 2013. `http://www.hamamatsu.com/resources/pdf/ssd/s12572-010_etc_kapd1045e.pdf`.

[11] N. Lalovic, J. Gerl, D. Rudolph, R. Hoischen, and P. Golubev. Simulations for position-sensitive tracking of γ rays in scintillators: Approach for source reconstruction. *GSI Scientific Report 2013, GSI Report 2014-1*, pages 123–124, 2014.